Acoustic metasurfaces and topological phononics for acoustic/elastic device design

Kenji Tsuruta*

Department of Electrical and Electronic Engineering, Okayama University, Okayama 700-8530, Japan.

E-mail: tsuruta@okayama-u.ac.jp

This paper reviews recent progress in acoustic metasurface and a novel concept denoted as topological acoustic/phononics for designing compact yet efficient acoustic devices. After a brief review of these research area and their impact on ultrasonic technologies, I first introduce some of our efforts to develop highly efficient sound absorption devices using acoustic metasurface. A resonance-based mechanism to achieve efficient absorption in the metasurface structures thinner than wavelength of the incident sound is briefly discussed and its extensions to broad spectrum are highlighted. Next a valley topological phononic system is introduced and its applications to the design of phononic waveguide are exemplified. I show the band structure design for extracting topologically protected edge mode as well as the numerical and experimental demonstration of the robustness of phononic waveguides constructed in both acoustic and elastic regimes.

1. Introduction

Artificially engineered subwavelength structures that response to electromagnetic waves in manners not found in nature, called metamaterials [1-6], have significantly broadened the range of research areas not only in electromagnetics but also mechanics [7-9], acoustics [10-16], seismology [17,18]. Especially, *acoustic metamaterials* have provided novel insights in the development of acoustic/elastic devices used in many industrial sectors. The ability to realize exotic responses to the incident sound, such as negative refractions [19-21], cavity resonances [22,23], and nonreciprocal propagations [24-26], has offered a novel design space in ultrasonic devices including ultrasonic lens, sound cloaking, and acoustic switch/diodes. Among them, active wavefront control and perfect sound absorption realized by acoustic metasurfaces have received much attention considering high demand of noise isolation in architectural and automotive applications [14,15].

Phononic crystal (PnC) [27-29], a composite structure made of materials with different elastic properties periodically arranged, has also shown promises in designing novel acoustic/elastic materials, especially as an analogy of photonic crystal (PtC) [30,31]. The frequency band structure in the reciprocal space provides the fundamental information that compasses to design wave propagation in the PtC/PnC. Some exotic responses to the incident sound, which are already mentioned above, can also be realized in PnC by designing the band structures. As a typical application of PnC to wave-propagation control is an acoustic waveguide. By introducing a cavity region at any place in the crystal, localized mode appears at a frequency within a band gap, which can be used for waveguide design. The waveguides thereby designed, however, suffer from strong degradation at corners and at defects along the path due to the backscattering. Rapid growth of research interest in another topic of the present review, topological phononics, was strongly due to this drawback in the PnC.

The emergence of topological physics based on the analogy of the electron wave function in the topological insulator [32-34] to the classical wave propagations [35-40] has recently initiated a new trend of the ultrasonic technology. These approaches have been examined and verified mainly within audible range (kHz) to ultrasonic wave (MHz) until now. Ability for the unidirectional propagation and/or the immunization to backscattering at defective area in the path and its possible extension to the extreme ultrasonic frequency regime (GHz) are keys to the realization of the next generation acoustic devices implemented in the Beyond 5G/6G information technologies.

In this paper, mainly based on our recent efforts, I try to review the research trends and the progresses on acoustic metasurfaces design and on topological physics approach for acoustic waveguide design utilizing the phase invariant of phonon band of PnC. As for the metasurfaces we focus specifically on a membrane type and a thin tubular type of metasurfaces and their application to sound absorber, whereas valley topological waveguide designs are discussed in the second topic of this review.

All the numerical calculations on eigen-mode analyses and the wave-propagation simulations presented in this paper have been performed by solving the linear elastic-wave equations based on the finite element method (FEM) using the software package COMSOL Multiphysics [41].

2. Acoustic metasurfaces

2.1 Resonator based implementation of metasurfaces

Recent attention on the metasurface has begun in the context of the generalization of Snell's law [42] applied to controlling light reflection/refraction on a surface by introducing the phase modulations/discontinuities induced resonantly by plasmonic nanostructures fabricated artificially on the surface [43,44]. This concept can be applied to tailoring wavefront on sound-wave refraction, as schematically illustrated in Fig.1. Modulation of the sound with longer wavelength than the thickness of the metamaterial is realized, for example, by tuning of the material's impedance through resonators built in the structure and by its nonuniform distribution [10]. Among the various attempts to realize such exotic acoustic properties, nearly perfect sound absorbers based on acoustic metasurfaces have been attracting much attention as a simple yet powerful scheme to design new acoustic devices for practical applications such as noise shielding. Different from conventional sound absorbers, which rely on materials loss and/or the interference with transmitted and reflected waves, the metasurface utilizes strong wave-matter interaction of resonators to achieve perfect impedance matching at the interface as well as to generate strong losses in the thin structure.

The (complex) acoustic impedance of a *m*th vibration mode Z_m can be expressed in general as

$$Z_m = i\left(\frac{\omega A_m}{\omega_m^2 - \omega^2 - i\beta\omega}\right)^{-1}, \tag{1}$$

where ω_m and A_m represent the eigen frequency and some relevant pre-factor (area per unit mass) of *m*th mode, respectively, in the resonator [13,15]. The highly efficient sound absorption requires that the perfect matching conditions with an incident wave from the air (impedance Z_0), expressed as

$$\mathrm{Im}(Z/Z_0) = 0 \ \text{ and } \ \mathrm{Re}(Z/Z_0) = 1, \tag{2}$$

are fulfilled, which is equivalent to the no-reflection condition $R = |(Z - Z_0)/(Z + Z_0)| = 0$.

2.2 Metasurface design based on membrane resonator

Above discussed metamaterials properties have been realized by the Decorated Membrane Resonators (DMR) [15,45] depicted in Fig.2(a). The high sound absorption occurs when the membrane and air layer vibrate to dissipate sound energy as heat. The natural vibration modes of the membrane are coupled with the air layer behind to generate a new vibration mode which leads to an efficient sound absorption. At the hybrid mode frequency, the membrane is displaced concentrically so that a solid button place at the center of the membrane can act as a piston to efficiently compress the air and large deformation of the membrane, and hence it leads to highly efficient energy dissipation, as shown in Fig.2(b).

The high efficiency for sound absorption of the DMR is achieved by the hybridization of vibration modes in the membrane and the backing air layer in the DMR. The (complex) acoustic impedance of the hybridized vibration mode can be expressed as

$$Z_h = Z_M + Z' . \tag{3}$$

In this expression,

$$Z_M = i\left(\sum_m \frac{1}{\langle\rho\rangle_m} \frac{\omega}{\omega_m^2 - \omega^2 - i\beta\omega}\right)^{-1}, \tag{4}$$

and $Z' = i\gamma p/(s\omega)$ are the impedance of the membrane and that of the air layer in the DMR, respectively. Here γ, p, s, ω represent the adiabatic index of air, an average pressure of the incident wave, the thickness of the air layer, and an angular frequency of vibration. The membrane impedance Z_M involves the dissipation coefficient β and mode-dependent parameters, *i.e.* the angular frequency ω_m and an effective mass density $\langle\rho\rangle_m$ of *m*th mode that is a weighted average with displacement of the mode. The highly efficient sound absorption occurs when the perfect matching conditions of the hybrid mode with an incident wave, expressed again in Eq. (2).

As an example, the lowest two membrane modes generate a hybrid mode which can be expressed approximately as

$$\omega_h^2 = \frac{1}{2}\left(\omega_1^2 + \omega_2^2 + \frac{\gamma p}{\langle\rho\rangle s}\right) - \frac{1}{2}\sqrt{(\omega_2^2 - \omega_1^2)^2 + \left(\frac{\gamma p}{\langle\rho\rangle s}\right)^2}, \tag{5}$$

where $\omega_h, \omega_i (i = 1,2)$, $\langle\rho\rangle$ are frequencies of the hybrid mode and *i*th membrane mode, and an average effective mass density of the modes. In Fig.3, the two-mode hybridization is demonstrated numerically by using a finite-element method (FEM) and compared with the frequency predicted analytically. The circular membrane made of polypropylene with diameter 30 mm and thickness 0.2 mm possesses the lowest concentric eigen modes at f_1 = 586 Hz [(0,1) mode] and f_2 = 2279 Hz [(0,2) mode] for the peripherally fixed condition. By giving a proper value for $\langle\rho\rangle$, one can approximately obtain the frequency for a hybrid mode via Eq. (5) to be 1193 Hz (f_h), whereas FEM calculation gives 1120 Hz in the case of incident pressure (p) of 1 Pa. It should be noted that there is a nonconcentric mode [(1,1) mode] between f_1 and f_2. However, this mode does not contribute to generate the sound-absorbing mode as its average displacement vanishes. Thus, it is essential to control number and position of the individual resonance mode of the membrane in order to design properly the absorption spectrum.

In spite of the nearly 100% sound absorption at the resonance frequency of the DMR, the very narrow spectrum hampers to apply the design concept to practical sound insulations, where the broader absorption spectrum is needed for efficient sound shielding [46]. We have recently proposed a novel metasurface structure which can exhibit broader absorption spectra [47]. Our approach is based on the multiplication of membrane modes by simply introducing an asymmetry in the membrane shape. Figure 4(a) shows designed structures with dimer and trimer shape of the circular membranes along with their absorption spectrum obtained by FEM simulations. The results show multiplexing and broadening of the absorption peak with the proposed DMR structures. This approach to broadening the absorption spectra is validated by experimental measurements. Figure 4(b) depicts 3D printed DMR structures with dimer and trimer membranes. Their absorption spectra for an incident wave are also plotted in Fig. 4(b). It has thus confirmed that our simple approach is effective to overcome the original drawback of DMR, that is, extremely narrow absorption spectrum.

2.3 Metasurface design based on split-tube resonator

Although the membrane resonators exemplified above have been proved to be effective, the absorption function in lower frequency range than 1000 Hz is desired for the metasurfaces in the practical applications such as those toward the environmental regulation against traffic noise. The low-frequency tunable acoustic absorber based on split tube resonators was originally proposed in order to meet such a demand [48]. The tubular resonator of elliptic cylinder with a side cut was examined, where polylactide (PLA) has been adopted for the base materials in order to reduce the total weight of the structure. The aluminum plate placed behind the tube has the role of reflecting sound waves which resonate with the sound absorber, as well as the role of preventing sound transmission. Figure 5(a) shows the basic structure (insets) and absorption coefficient of the single split-tube resonator. The wavelength of the sound wave of 516 Hz , at which the sound absorption peak in Fig. 5(a), was about 660 mm, whereas the thickness of the sound absorbing structure including the split tube and the aluminum plate was 25 mm. The high sound absorption characteristic was thereby demonstrated even in low-frequency sounds where sound absorption is generally difficult due to the large difference in size between the wavelength and the structure. The position of resonance peak can be estimated as an elastic vibration of the split tube coupled with the air layer in the tube as a Helmholtz-like resonance, as schematically illustrated in Fig. 5(b). The efficient absorption occurs based on conversion of the sound energy into heat energy through the hybrid resonance.

Despite that it achieves nearly 100% sound absorption at relatively low frequency, the sharp peak at the resonant frequency hampers to utilize the structure in practical applications that have ambient sound environments with relatively wide frequency spectra. To solve the problem of narrow frequency spectrum, we again adopted the method of superposition of peaks by multiplexing the split tubes with different size [47]. By numerical simulation, we have examined the dependence on the number of layers of the tube from two through six. From the results of each multiply layered tube, two types of sound absorption peaks were obtained: a single-mode sound absorption peak in which each tube vibrates nearly independently, and a hybrid-mode sound absorption peak in which all the layers vibrate. Figure 6 reveals that the sound absorption peaks due to the single vibration modes appear at the frequencies in lower frequency range than 495 Hz, whereas the peaks at the higher frequencies than 495 Hz are attributed to excitations of the hybrid modes. Thus, the multiple mode generation can be demonstrated by the thin split-ring tube via hierarchical hybridization of resonance.

3. Topological phononics

3.1 Topology in acoustic/elastic systems

Another topic discussed in this review is topological physics approach to designing acoustic/elastic wave devices. The predictions and discoveries of the spin Hall effect [51,53] and topological insulators [54,55] have stimulated the search for analogous topological states in classical systems such as light [35-37], sound [38-40], and mechanical waves [39], especially after the Nobel prize in physics was awarded to three theoretical founders of the topological physics in condensed-matter physics [56].

Topological invariance in dispersion curves drawn in the reciprocal ($\boldsymbol{k}$) space is hold also in the classical systems [36,38]. Let us write a wave equation of a periodic system in general form as

$$\hat{\mathcal{L}}\psi(\boldsymbol{r}) = \omega^2\psi(\boldsymbol{r}) \text{ with } \hat{\mathcal{L}}(\boldsymbol{r}+\boldsymbol{a}) = \hat{\mathcal{L}}(\boldsymbol{r}). \quad (6)$$

Invoking the Bloch's theorem, the *n*th eigen function can also be written as

$$\psi_{\boldsymbol{k}}^n(\boldsymbol{r}) = u_{\boldsymbol{k}}^n(\boldsymbol{r})e^{i\boldsymbol{k}\cdot\boldsymbol{r}}. \quad (7)$$

The Bloch state $u_{\boldsymbol{k}}^n(\boldsymbol{r})$ also obeys the same periodicity as the system as

$$u_{\boldsymbol{k}}^n(\boldsymbol{r}+\boldsymbol{a}) = u_{\boldsymbol{k}}^n(\boldsymbol{r}). \quad (8)$$

The physical property of the eigenstate is characterized in part by its dispersion relation between $\omega_n(\boldsymbol{k})$ and $\boldsymbol{k}$, but also by *topological* quanta, such as the Berry phase defined as

$$\phi_n \equiv \oint \boldsymbol{A}_n(\boldsymbol{k})\cdot d\boldsymbol{k} = \iint \boldsymbol{\nabla}_{\boldsymbol{k}} \times \boldsymbol{A}_n(\boldsymbol{k})\cdot d\boldsymbol{S}, \quad (9)$$

where

$$\boldsymbol{A}_{\boldsymbol{k}} \equiv i\langle u_{\boldsymbol{k}}^n | \boldsymbol{\nabla}_{\boldsymbol{k}} u_{\boldsymbol{k}}^n\rangle \quad (10)$$

is the Berry connection. The integrant in Eq. (9),

$$\boldsymbol{B}_n(\boldsymbol{k}) = \boldsymbol{\nabla}_{\boldsymbol{k}} \times \boldsymbol{A}_n(\boldsymbol{k}) \quad (12)$$

is called the Berry curvature. This has analogous form as the magnetic flux in real space given that the Berry connection holds a similar physical property as a gauge-variant vector potential under a gauge transformation $u_{\boldsymbol{k}}^n(\boldsymbol{r}) \to u_{\boldsymbol{k}}^n(\boldsymbol{r})e^{i\phi_n}$. The single valuedness of $e^{i\phi_n}$ for a given closed path defines an invariant modulo 2π of ϕ_n for the Bloch state.

As for acoustic cases, the wave equation for a scaler quantity ψ in a fluid (pressure) or an isotropic solid (one-dimensional displacement) can be represented in the form

$$\rho\frac{\partial^2\psi}{\partial t^2} = \boldsymbol{\nabla}\cdot(K\boldsymbol{\nabla}\psi) \quad (13)$$

where ρ and K are mass density and elastic modulus. When the system has periodicity in $\rho(\mathbf{r})$ and $K(\mathbf{r})$, the Bloch' theorem is hold in its eigenstate specifying the Bloch state $u_{\boldsymbol{k}}^n(\boldsymbol{r})$. The PnC is such a system. The dispersion relation between eigen frequency and wave vector provides rich information helpful in designing acoustic properties, such as band gap, cavity state, and negative effective masses, and so on. Moreover, as discussed above, the characteristics of the Bloch state can also be captured by its topological features such as the Berry phase and the Berry curvature.

When the phononic system has a band gap in its dispersion relation and has eigenstates with two different topologies near the band gap, and there exists bands which show the phase transition of their band topology while the structure is continuously changed. Figure 7(a) illustrates a schematic of phononic bands and localized propagation modes (edge modes), depicted in red and blue lines, generated at the interface between bands with different phases (ϕ). Transmission characteristic with very small loss is obtained at the frequency within the red dashed circle in the figure due to the propagation through this topologically protected state. In two-dimensional phononic structures, the hexagonal symmetry is often adopted to express the edge state in the band gap. In the system with C_{3v} symmetry, the Brillouin zone has the hexagonal shape and gap closing (the Dirac point) occurs at the K points. Also, the Berry curvature in the Brillouin zone of such a system has peaks at K points. Thus, the edge modes appear in the gap near the K point, not Γ point. Such a topological feature is called to be valley-topological. One can define a topologically invariant value called valley Chern number obtained by integrating the Berry curvature around each Dirac point. If the Berry curvature at a K point has opposite sign with the neighboring K points, as schematically shown in Fig. 7(b), it has been shown that the edge states in the gap appears at an interface between two hexagonal PnCs with the valley Chern numbers of the sign opposite to each other at each corresponding K point. Such an interface can be an efficient waveguide. In the following sections I show this concept is applied to the topological acoustic waveguide design in the phononic structure and demonstrate numerically and experimentally that robust wave transmission, *i.e.,* immune to backscattering by defects and/or corners in the waveguide, is possible even in the waveguides with complex propagation paths as long as the edge mode is properly excited in the paths.

3.2 Design of valley topological acoustic waveguide

Many of valley topological systems in 2D proposed and examined previously have C_{3v} symmetry realized by the unit-cell structure with triangular elements [57-60]. On the other hand, we have recently proposed a new structure that can be easily fabricated yet retains C_{3v} symmetry by using three rods with circular cross section in the unit cell, as illustrated in Fig. 8(a) [61,62]. The center-of-mass of the three rods is located at hexagonal lattice points. The three rods are made of stainless steel and embedded in water. The arrangement of the three rods assures the unit cell to be C_{3v} symmetric possessing the Dirac point at K points, and the rotation angle α is defined as a parameter to specify the phase of the system. Figure 8(b) shows the eigenmodes and band diagrams of the three rods unit cell. It shows that K^+ mode and K^- mode appear at the K point in the band diagram for the structure of $\alpha = -30°$ and 30°, respectively. By continuously changing α from −30° (left) to 30° (right), the gap is narrowed and closed at α =0° having the Dirac-like cone, exhibiting the topological phase transition where the topologies of upper and lower bands than the gap are flipped.

We construct an acoustic waveguide with the topological phononic supercell created by arranging unit cells composed of three rods with α=–30° in the lower layer and α=30° in the upper layer. The lattice constant of the PnC structure is a = 2.2 mm. Figure 9(a) shows band structure of supercell with unit cells of α=–30° in the lower layer and α=30° in the upper layer. The eigenmode analysis of this supercell reveals that the edge state appears at the frequency around 400 kHz. Figure 9(b) shows sound pressure distribution (absolute value) in straight waveguide with three rods valley-type phononic crystals for 400 kHz incident wave. The sound wave propagates on the boundary efficiently through the topologically protected edge mode.

Figure 9(c) shows the band structure for the supercell which combines two unit cells of $\alpha = -30°$and $\alpha = 30°$ with the interface perpendicular to the Γ-K direction. Figure 9(d) shows sound pressure distribution (absolute value) in the crank-shaped acoustic waveguide with the three rods valley-type topological structure for 400 kHz incident wave. The sound wave propagates on the boundary between two topologically inverted phononic structures with the cranked shape.

Based on the results of the 2D FEM simulation described above, we fabricated a three rods valley topological waveguide in 3D. Figure 10(a) is a photograph of the fabricated acoustic waveguide of three rods valley topological phononic crystals with a crank-shaped interface. The waveguide is fabricated by inserting stainless rods into a 3D printed mold. In contrast to other works based on the equilateral triangle valley-type structure, it does not require metal processing and can thus be fabricated easily. We measured sound pressure in water using the fabricated waveguide. The experimental setup in the present study is illustrated in Fig. 10(b). Figure 10(c) shows transmission in the FEM simulation and in the experiment for the crank-shaped three rods valley-type topological acoustic waveguide. From Fig. 10(c), both the experimental and simulation results verified the high robustness of the valley phononic waveguide for the incident wave around 400 kHz.

3.3 Valley topological elastic waveguide

Wave propagation in the 2D acoustic systems exemplified above is inherently limited within longitudinal modes. In view of further applications by implementing the functionality into on-chip systems, the phononic systems should be designed in 3D solid-state media. Here, topological phononic structure in a thin plate and the edge mode of an elastic wave are designed for developing an efficient elastic waveguide. The realization of next-generation mobile communication devices relies on the development not only of high-speed logic gates but also of efficient signal processing components such as the Surface Acoustic Wave (SAW) filters.

The phononic structure adopted here consists of a 3D unit cell with snowflake-shaped holes in a hexagonal grid, as illustrated in Fig. 11(a) [63]. A valley-shaped band structure can be varied by changing the length of the six legs of the snowflake (Δr). The snowflake-like unit cells have been adopted in variety of study for phononic crystals as a simple but highly controllable structural unit in designing phonon band structure [64-67].

Figure 11(b) shows the band diagram of a phononic structure with a snowflake-shaped unit cell, revealing that the bandgap opens at $\Delta r = \pm 1.76\ \mathrm{mm}$. Although the two eigenmodes have similar shapes, the vortex directions of the mechanical energy flow are opposite to each other. It can also be seen that the direction of the vortices changes above and below the band at Δr=0. Since this indicates a topological phase transition, we can expect valley chiral edge states to appear around this frequency [57]. From Fig. 11(b), we confirmed that the phonon-band topological phase transition in the PnC on thin plate occurs in reciprocal space and can be easily controlled by a single parameter Δr.

We then designed and examined a Z-shaped waveguide and its transmission properties for an incident wave. As the interface along the oblique line in the Z shape have same type of the symmetry as that along the horizontal lines, these waveguides were used to assess the robustness of wave propagation against back scatterings by the corners of the paths. Figure 12(a) illustrates the designed waveguides along the interfaces between phononic structure with different Δr. [$\Delta r = +1.76\ \mathrm{mm}$ and $-1.76\ \mathrm{mm}$.]

Next, topological Z-shaped waveguides made of polypropylene were fabricated by using a 3D printer, as depicted in Fig.12(b). The induced elastic waves at the entrance of the waveguide were measured and mapped with a laser Doppler vibrometer. Figure 12(c) depicts spacial distributions of the displacement. The large displacement was observed only along the interface regions indicating highly efficient wave propagation is realized, as predicted in the numerical simulations.

Recently, a degradation of robustness by the presence of corners and/or structural randomness has been quantitatively evaluated in terms of the "back scattering length" ξ in valley topological photonic waveguides [68-70]. The same evaluation in terms of ξ should be valid in the valley topological phononic waveguide. Figure 12(d) show logarithmic plots of the transmittance along the paths of the Z-shaped waveguides in the experiment. The values of ξ are evaluated from the negative slope of the logarithmic plot ($\xi \sim -x/\log T$) for each segment AB and CD to give approximately 365 and 285, respectively. On the other hand, at B and C (corners in the waveguides), have a smaller ξ (~100) than the formers. This indicates that the effect of back scattering is more pronounced in corner sections than the structural randomness in the straight sections. The attribution of the lower values of the Z-shaped topological waveguide than that of the straight topological waveguide is thereby identified quantitatively. Despite that the immunization of back scattering is shown to be degraded, the present values of around 300 in the straight waveguides prove eminent efficiency compared to the reported values (~100) in valley-topological photonic systems [68,69]. This may imply that surface acoustic waves can hold higher efficiency in the transmission than photonic circuits in utilizing topological waveguides.

Recently, further attempts have been made to control elastic waves at ultra-high frequency regime (GHz) in thin films with phononic crystals [23,71-73]. Moreover, in view of further development beyond the current telecommunication frequency (6G), nanoscale phononic design toward THz frequency range, which may reach to atomistic level [74,75], should be within a scope [76]. Here we preliminary examined topological waveguides for this purpose. Figures 13(a) and 13(b) present trial design of Z-shape and double Z-shaped waveguides designed on GaAs substrates with μm- and nm-scale phononic structures, respectively. Also shown are displacement fields in the FEM simulations for the incident waves depicted in the figures. It thus reveals that topologically protected elastic wave can also be excited and propagate efficiently along the interfaces. These analyses clearly indicate that the design scheme based on the band analysis to find topological phase transition is effective even in these nanometer scales.

4. Conclusions

In this paper, I introduced some topics on the recent advances in acoustic metasurfaces, and in topological phononics/acoustics, which were partly presented in the 43rd Symposium on Ultrasonic Electronics (USE2022) and its Proceedings volume [77]. The design scheme for resonator-based metasurfaces and its applications to sound absorbing structures (the DMR and the split-tube resonator) are proposed, emphasizing the possible broadening by multiplexing of their resonant modes. The metasurface approach can be specifically useful to develop a noise-shielding material used in *e.g.*, electric vehicle in which light weight yet high performance in noise shielding is required. As for topological phononics, highly efficient transmission in the topological waveguides was demonstrated by both numerical simulations and experiments. The band topology was proven to be powerful tool in designing acoustic/elastic waveguide implemented especially in SAW devices. In actual design, however, the band design still involves trial-and-error processes, especially for searching the topological phase transition that is a key to constructing the interface where the topologically protected edge mode appears. Theoretical and/or computational methodology to systematically identify the topological index (Berry phase) for arbitrary PnC structure should be developed to accelerate the device developments. Also, high demands are expected in the extension of the methodology presented here to higher frequency region toward the next-generation (6G and beyond) communication era [76]. Researchers in the fields of ultrasonic electronics should play a central role in responding to this demand.

Acknowledgments

I am grateful for helpful discussions, guidance, and collaborative works related to this study provided by collaborators, namely, Profs. Satoshi Iwamoto, Jun Kondoh, Osamu Matsuda, Masaaki Misawa, Masahiro Nomura, Keiji Sakai, Motonobu Tomoda, Oliver B. Wright, Ken Yamamoto, and Drs. Daiki Hatanaka, Atsushi Ishikawa, Hiroshi Yamaguchi, as well as present/former graduate students in Okayama University. This work was supported in part by the JSPS KAKENHI Grant Numbers JP21H05020 and JP21K18877.

References

[1] V. G. Veselago, *Sov. Phys. Uspekhi-USSR* **10,** 509 (1968).

[2] J. B. Pendry, A. J. Holden, W. J. Stewart, and I. Youngs, *Phys. Rev. Lett.* **76,** 4773 (1996).

[3] D. R. Smith, W. J. Padilla, D. C. Vier, S. C. Nemat-Nasser, and S. Schultz, *Phys. Rev. Lett.* **84,** 4184 (2000).

[4] D. R. Smith, J. B. Pendry, M. C. Wiltshire, *Science* **305**, 788 (2004).

[5] C. Caloz and T. Itoh, Electromagnetic Metamaterials: Transmission Line Theory and Microwave Applications, Hoboken, NJ, USA:Wiley, NOV. 2005.

[6] A. Ishikawa, T. Tanaka, and S. Kawata, *Phys. Rev. Lett.* **95**, 23740 (2005).

[7] R. Lakes, *Science* **235,** 1038–1040 (1987).

[8] X. Zheng, H. Lee, T.H. Weisgraber, M. Shusteff, J. DeOtte, E. B. Duoss, J. D. Kuntz, M. M. Biener, Q. Ge, J. A. Jackson, S. O. Kucheyev, N. X. Fang, and C. M. Spadaccini, *Science* **344**, 1373 (2014).

[9] T. Frenzel, M.Kadic, and M. Wegener, *Science* **358**, 1072 (2017).

[10] D. Torrent and J. Sánchez-Dehesa, *New J. Phys.* **10**, 063015 (2008).

[11] S. Cummer, J. Christensen, and A. Alù, *Nat. Rev. Mater* **1**, 16001 (2016).

[12] M. R. Haberman and M. D. Guild, *Phys. Today* **69**, 42 (2016).

[13] G. Ma and P. Sheng, *Sci. Adv.* **2**, e150159 (2016).

[14] F.Zangeneh-Nejad and R. Fleury, *Rev. Phys*. **4**, 100031 (2019).

[15] J. Li, X. Wen, and P. Sheng, *J. Appl. Phys*. **129**, 171103 (2021).

[16] N. Gao, Z. Zhang, J. Deng, X. Guo, B. Cheng, and H. Hou, *Adv. Mater. Technol.* **7**, 2100698 (2022)

[17] A. Colombi, S. Guenneau, P. Roux, and R.V. Craster, *Sci. Rep.* **6**, 25320 (2016)

[18] O. Casablanca1, G. Ventura, F. Garescì1, B. Azzerboni1, B. Chiaia2, M. Chiappini, and G. Finocchio, *J. Appl. Phys.* **123**, 174903 (2018).

[19] J. Li, Z. Liu, and C. Qiu, *Phys. Rev. B* **73**, 054302 (2006).

[20] J. Han, T. Wen, P. Yang, and X. Zhang, *AIP Adv.* **4**, 057126 (2014).

[21] K. Manabe, A. Ishikawa, K. Yamamoto, T. Kanda, and K. Tsuruta, *Proc. IEEE Int'l Ultrasonics Sympo. (IEEE-IUS2018)*, 8580129 (2018).

[22] S. Mohammadi, A. A. Eftekhar, W. D. Hunt, and A. Adibi, *Appl. Phys. Lett.* **94**, 051906 (2009).

[23] D. Hatanaka and H. Yamaguchi, *Phys. Rev. Appl.* **13**, 024005 (2020).

[24] V. F. Nesterenko, C. Daraio, E. B. Herbold, and S. Jin, *Phys. Rev. Lett.* **95**, 158702 (2005).

[25] B. Liang, X. S. Guo, J. Tu, D. Zhang, and J. C. Cheng, *Nat. Mater.* **9**, 989 (2010).

[26] A. Ishikawa and K. Tsuruta, *Jpn. J. Appl. Phys.* **57**, 07JB01 (2017).

[27] M. S. Kushwaha, P. Halevi, L. Dobrzynski, and B. Djafari-Rouhani, *Phys. Rev. Lett.* **71**, 2022 (1993).

[28] M. S. Kushwaha, *Mod. Phys. Lett. B* **30**, 1630004 (2016).

[29] T.Vasileiadis, J. Varghese, V. Babacic, J. Gomis-Bresco, D. N. Urrios, and B. Graczykowski , *J. Appl. Phys.* **129**, 160901 (2021).

[30] K. Ohtaka, *Phys. Rev. B* **19**, 5857 (1979).

[31] J. D. Joannopoulos, R. D. Meade, and J. N. Winn, *Photonic Crystals*, Princeton University Press (1995).

[32] M.Z. Hansen and C.L. Kane, *Rev. Mod. Phys*. **82**, 3045 (2010).

[33] X.-L. Qi and S.-C. Zhang, *Rev. Mod. Phys.* **83**, 3045 (2011).

[34] Y. Tokura, K. Yasuda, and A. Tsukazaki, *Nat. Rev. Phys.* **1**, 126 (2019).

[35] L. Lu, J. Joannopoulos, and M. Soljačić, *Nat. Photon.* **8**, 821 (2014).

[36] T. Ozawa, H. M. Price, A. Amo, N. Goldman, M. Hafezi, L. Lu, M. C. Rechtsman, D. Schuster, J. Simon, O. Zilberberg, and I. Carusotto, *Rev. Mod. Phys.* **91**, 015006 (2019).

[37] S. Iwamoto, Y. Ota, and Y. Arakawa, *Opt. Mater. Exp.* **11**, 319 (2021).

[38] X. Zhang, M. Xiao, Y. Cheng, M.-H. Liu, and J. Christensen, *Commun. Phys*. **1**, 97 (2018)

[39] G. Ma, M. Xiao, and C. T. Chan, *Nat. Rev. Phys.* **1**, 281(2019).

[40] Y. Liu, X. Chen, and Y. Xu, *Adv. Funct. Mater.* **30**, 1904784 (2020).

[41] COMSOL Multiphysics® www.comsol.com. COMSOL AB, Stockholm, Sweden.

[42] N. Yu, P. Genevet, M. A. Kats, F. Aieta, J.-P. Tetienne, F. Capasso, Z. Gaburro, *Science* **334,** 333 (2011).

[43] T. Yatooshi, A. Ishikawa, and K. Tsuruta, *Appl. Phys. Lett.* **107**, 053105 (2015).

[44] G. Yoon, T. Tanaka, T. Zentgraf, and J. Rho, *J. Phys. D: Appl. Phys.* **54**, 383002 (2021).

[45] G. Ma, M. Yang, S. Xiao, Z. Yang, and P. Sheng, *Nat. Mater.* **13**, 873 (2014).

[46] C. Fu , X. Zhang, M. Yang, S. Xiao, and Z. Yang, *Appl. Phys. Lett.* **110**, 021901 (2017).

[47] K. Watanabe, M. Fujita, and K. Tsuruta, *Jpn. J. Appl. Phys.* **59**, SKKA06 (2020).

[48] X. Wu, C. Fu, X. Li, Y. Meng, Y. Gao, J. Tian, L. Wang, Y. Huang, Z. Yang, and W. Wen , *Appl. Phys. Lett.* **109**, 043501 (2016).

[49] S. Takasugi, K. Watanabe, M. Misawa and K. Tsuruta, *Jpn. J. Appl. Phys.* **60**, SDDA01 (2021).

[50] L. Jing, J. H. Wu, D. Guan, and N. Gao, *J. Appl. Phys.* **116**, 103514 (2014).

[51] M. I. Dyakonov and V. I. Perel, *Phys. Lett. A* **35**, 459 (1971).

[52] A. A. Bakun, B. P. Zakharchenya, A. A. Rogachev, M. N. Tkachuk, V. G. Fleisher, *Sov. Phys. JETP Lett.* **40**, 1293 (1984).

[53] Y. Kato, R. C. Myers, A. C. Gossard, D. D. Awschalom, *Science* **306**, 5703 (2004).

[54] C.L. Kane, E.J. Mele, *Phys. Rev. Lett.* **95**, 14 (2005).

[55] M. König, S. Wiedmann, C. Brüne, A. Roth, H. Buhmann, L.W. Molenkamp,X.-L. Qi, S.-C. Zhang, *Science* **318**, 766–770 (2007).

[56] https://www.nobelprize.org/prizes/physics/2016/summary/

[57] J. Lu, C. Qiu, L. Ye, X. Fan, M. Ke, F. Zhang, and Z. Liu, *Nat. Phys.* **13**, 369 (2017).

[58] D Jia, H.-X. Sun, J.-P. Xia, S.-Q. Yuan, X.-J Liu, and C. Zhang, *New J. Phys.* **20**, 093027 (2018).

[59] J. Wang and J. Mei, *Appl. Phys. Express* **11,** 057302 (2018).

[60] I. Kim, Y. Arakawa, and S. Iwamoto, *Appl. Phys. Expres*s **12**, 047001 (2019).

[61] K. Okuno and K. Tsuruta, *Jpn. J. Appl. Phys.* **59**, SKKA05 (2020).

[62] M. S. Ali, M. Kataoka, M. Misawa, and K. Tsuruta, *Jpn. J. Appl. Phys.* **62**, SJ1002 (2023).

[63] M. Kataoka, M. Misawa, and K. Tsuruta, *Symmetry* **14**, 2133 (2022).

[64] 29 M. G. Baboly, C.M. Reinke, B. A. Griffin, I. El-Kady, and Z. C. Leseman, *Appl. Phys. Lett.* **112**, 103504 (2018).

[65] J. Luo, L. Feng, and H. Huang, *J. Chen, Phys. Lett A*, **38**, 125974 (2019).

[66] D. Hatanaka and H. Yamaguchi, *Phys. Rev. Appl.* **13**, 024005 (2020).

[67] H. M. Masrura, A. Kareekunnan, F. Liu, S. G. Ramaraj, G. Ellrott, A.M.M. Hammam, M. Muruganathan, and H. Mizuta, *Micromachines* **11**, 655 (2020).

[68] B. Orazbayev and R. Fleury, *Nanophotonics* **8**, 1433 (2019).

[69] G. Arregui, J. Gomis-Bresco, C. M. Sotomayor-Torres, and P. D. Garcia, *Phys. Rev. Lett.* **126**, 027493 (2021).

[70] M. Patterson and S. Hughes, *Phys. Rev. Lett.* **102**, 253903 (2009).

[71] P. H. Otsuka, S. Mezil, O. Matsuda, M. Tomoda, A.A. Maznev, T. Gan, N. Fang, N. Boechler, V.E. Gusev, and O. B. Wright, *New. J. Phys*. **20**, 013026 (2018).

[72] H. Takeshita, M. Misawa, and K. Tsuruta, *Proc. Symp. Ultrason. Electron.* **42**, 3Pb1-2 (2021).

[73] Q. Zhang et al., D. Lee, L. Zheng, X. Ma, S.I. Meyer, L. He, H. Ye, Z. Gong, B. Zhen, K. Lai, and A.T.C. Johnson, *Nat. Elec.* **5**, 157 (2022).

[74] R. Hikata, K. Tsuruta, A. Ishikawa, and K. Fujimori, *Jpn. J. Appl. Phys.* **54**, 07HB07 (2015).

[75] J.-W. Jiang, B-S. Wang, and H. S. Park, *Nanoscale* **10**, 13913 (2018).

[76] A. Kumar, M. Gupta, P. Pitchappa, N. Wang, M. Fujita, and R. Singh, *J. Appl. Phys.* **132**, 140901 (2022).

[77] K. Tsuruta, Proc. Symp. Ultrason. Electron. **43**, 1PL (2022).

Figure Captions

Fig. 1. Schematic of an acoustic metasurface with a wavefront controllability for an incident wave.

Fig. 2. (a) A schematic of the DMR and its cross-sectional view. (b) The sound absorption coefficient and the mode profile of the membrane at the peak frequency. (Adapted from Ref. 47)

Fig. 3. An example of hybrid-mode generation. The 1st and 2nd fundamental eigen modes with 586 Hz and 2272 Hz are coupled with an air layer leading to generate a hybridized mode at 1120 Hz, which is approximately predicted by Eq. (5).

Fig. 4. (a) Sound absorption and mode diagram with dimer (left) and trimer (right) membranes structures. (b) Fabricated structures (left) and absorption spectra (right) for respective structures in numerical simulations and experimental measurements. (Adapted from Ref. 47)

Fig. 5. (a) Cross-sectional view, absorption spectrum, and resonance mode at 516 Hz of a split tube. (b) A schematic of hybridization mechanism of elastic vibration of the tube with the air layer in the tube.

Fig. 6. (a) The sound absorption spectrum of six-layer split tubes, and (b) the mode shapes and displacements at each corresponding peak in the spectrum. (Adapted partially from Ref. 49)

Fig. 7. (a) Schematics of topological phase transition in phononic band and an edge mode generated at the interface between bands with different topological phases (ϕ). (b) A schematic of the Berry curvature distribution in a phononic structure with C_{3v} symmetry.

Fig. 8. (a) Unit cell structure (b) phonon band structure of three rods valley-type phononic crystal. (Adapted from Refs. 61 and 62)

Fig. 9. (a) Band structure of supercell combining two unit cells of α=–30 °and α=30° with the interface along Γ-K direction. The solid red circle indicates upper band edges near the edge states where two bands cross each other. (b) Sound pressure distribution (absolute value) in straight waveguide for 400 kHz incident wave. (c) Band structure of supercell combining two unit cells of α=–30 ° and α=30° with the interface perpendicular to the Γ-K direction. (d) Sound pressure distribution (absolute value) in crank-shaped waveguide for 400 kHz incident wave. (Adapted from Ref. 61).

Fig. 10. (a) Crank-shaped three rods valley-type topological acoustic waveguide fabricated in a resin template. (b) Schematic of experimental setup. (c) Transmission spectra measured in simulation and experiment of crank-shaped three rods valley-type topological acoustic waveguide. (Adapted from Ref. 61).

Fig. 11. (a) Snowflake-like unit-cell structure in a phononic crystal and (b) phonon band diagrams and eigenmodes at K points for three unit-cell structures with different Δr. (Adapted from Ref. 63).

Fig. 12. Structures and displacement fields in numerical simulation for incident wave at 84.2 kHz in Z-shaped topological waveguides between the unit cells of $\Delta r = \pm 1.76$ mm, and (b) its fabricated sample. (c) Distribution of normalized displacement and (d) logarithmic plot of the transmittance along the path of the Z-shaped waveguide obtained by a laser-doppler measurement. The points designated by A, B, C, and D in Fig. 12(d) correspond to the points in Fig. 12(b). (Adapted from Ref. 63)

Fig. 13. Unit-cell structures and out-of-plane displacements in finite-element simulation of topological phononic waveguides fabricated in GaAs membranes **(a)** with μm-scale and **(b)** with nm-scale lattice constant. The incident-wave frequencies to the waveguide are (a) 0.78 GHz and (b) 0.91 THz, respectively.

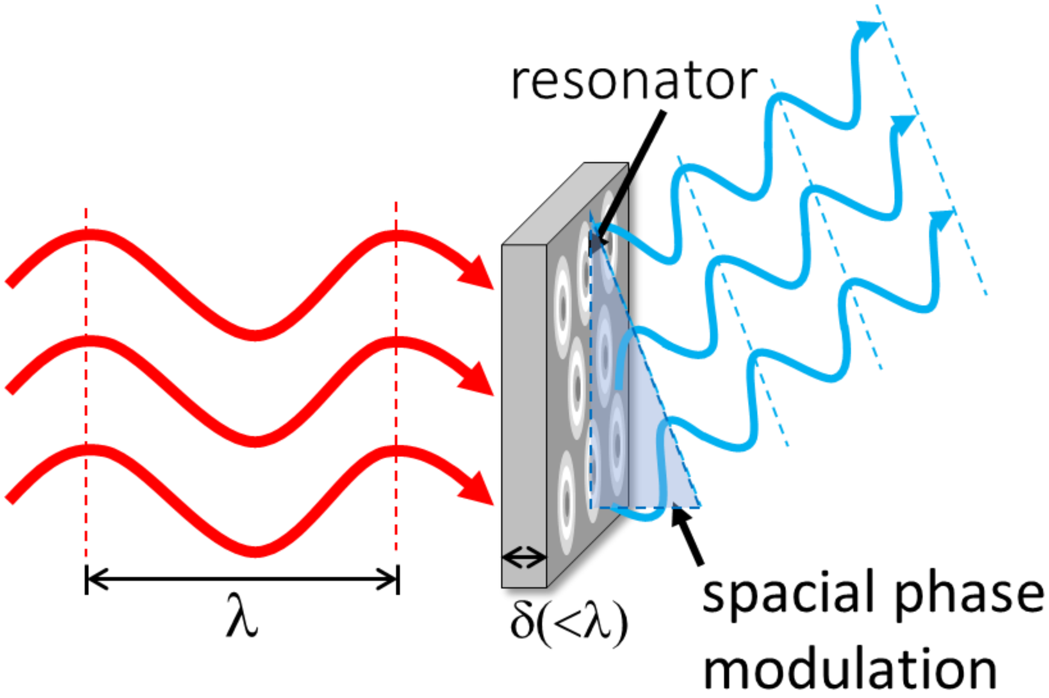

Fig.1.

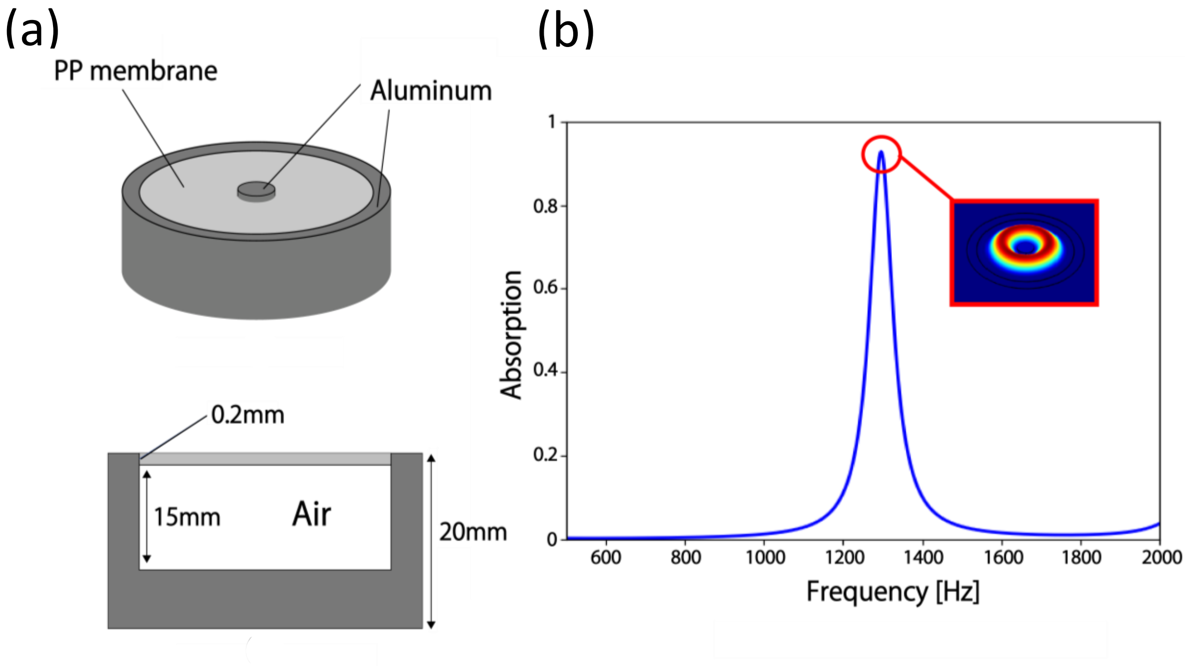
(a)
PP membrane
Aluminum
0.2mm
15mm
Air
20mm
(b)
Absorption
Frequency [Hz]
0
0.2
0.4
0.6
0.8
1
600
800
1000
1200
1400
1600
1800
2000

Fig. 2.

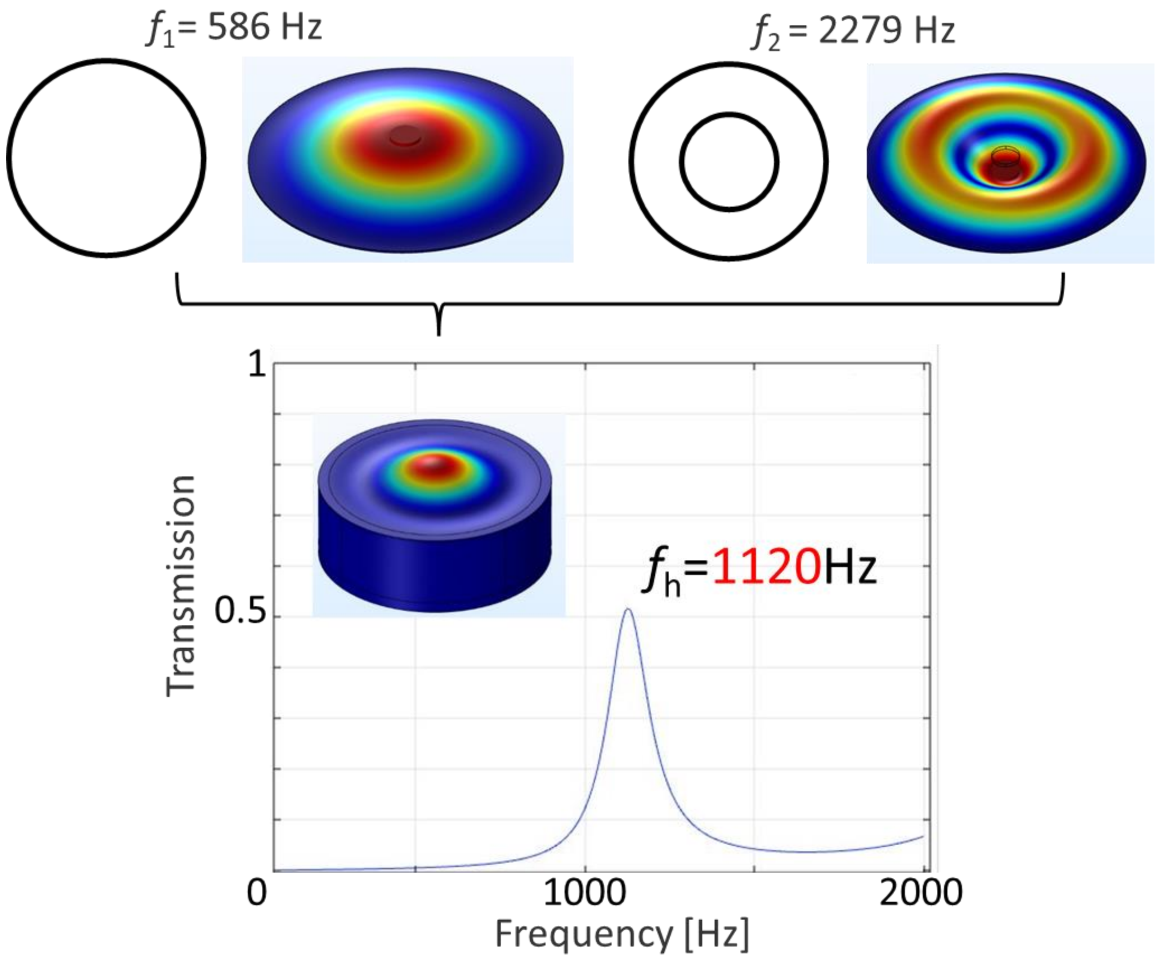

f_1= 586 Hz
f_2 = 2279 Hz
1
0.5
0
Transmission
f_h=1120Hz
1000
2000
Frequency [Hz]

Fig. 3.

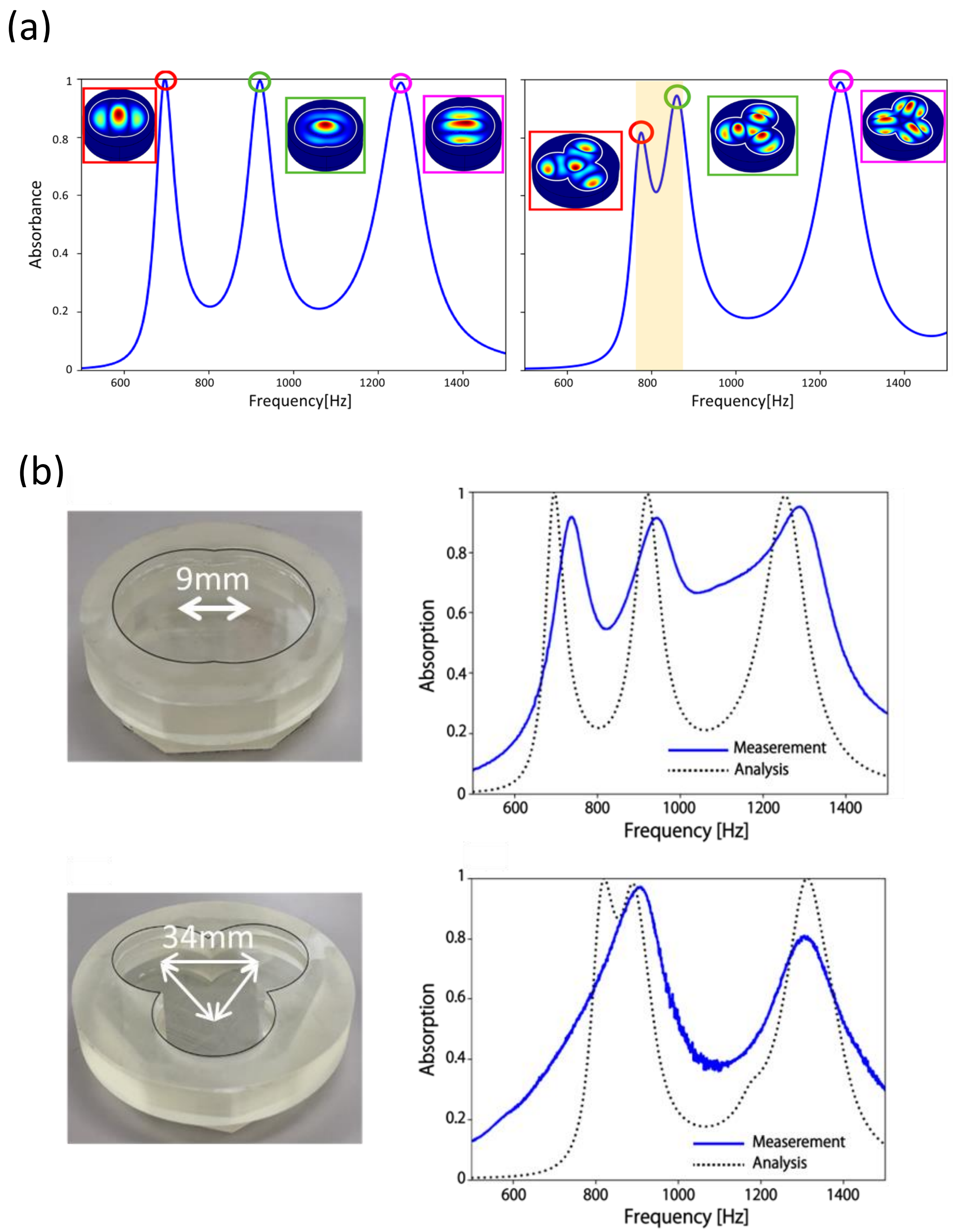

(a)
Absorbance
Frequency[Hz]
Frequency[Hz]
(b)
9mm
34mm
Absorption
Frequency [Hz]
Measerement
Analysis

Fig. 4.

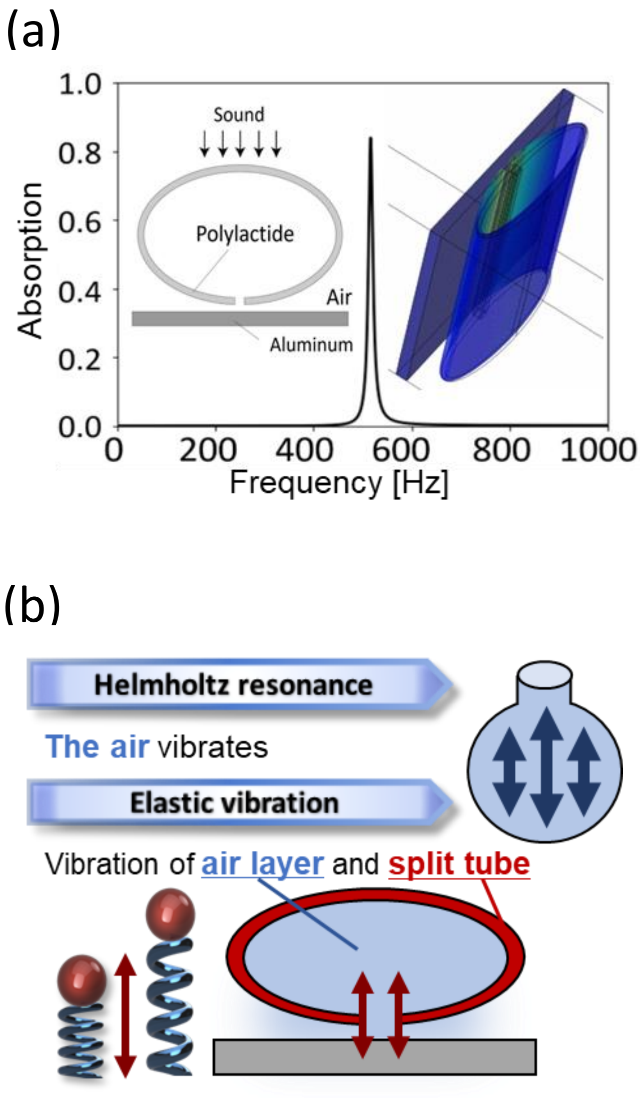
(a)
1.0
0.8
0.6
0.4
0.2
0.0
Absorption
Sound
Polylactide
Air
Aluminum
0
200
400
600
800
1000
Frequency [Hz]
(b)
Helmholtz resonance
The air vibrates
Elastic vibration
Vibration of air layer and split tube

Fig. 5.

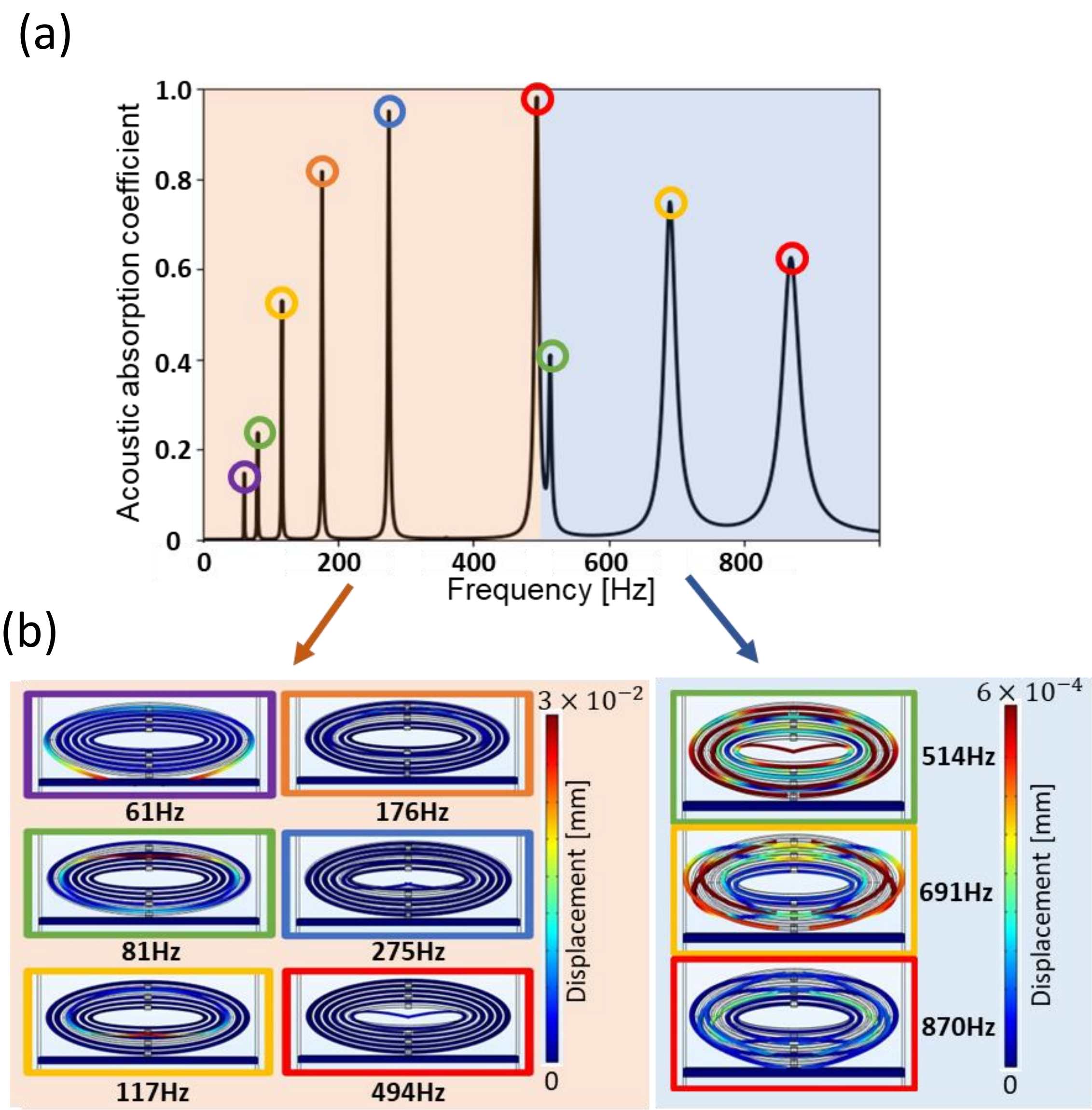

(a)
1.0
0.8
0.6
0.4
0.2
0
Acoustic absorption coefficient
0
200
400
600
800
Frequency [Hz]
(b)
61Hz
176Hz
81Hz
275Hz
117Hz
494Hz
3×10^{-2}
Displacement [mm]
0
514Hz
691Hz
870Hz
6×10^{-4}
Displacement [mm]
0

Fig. 6.

(a)

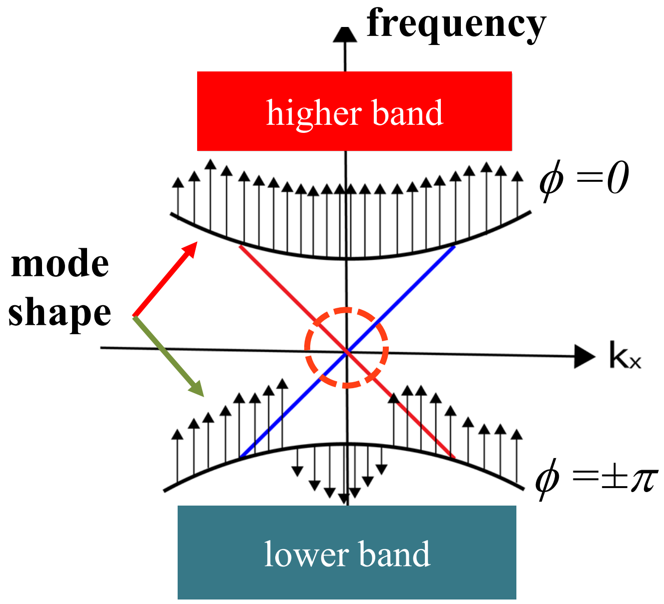
frequency
higher band
ϕ =0
mode
shape
kx
ϕ =±π
lower band

(b)

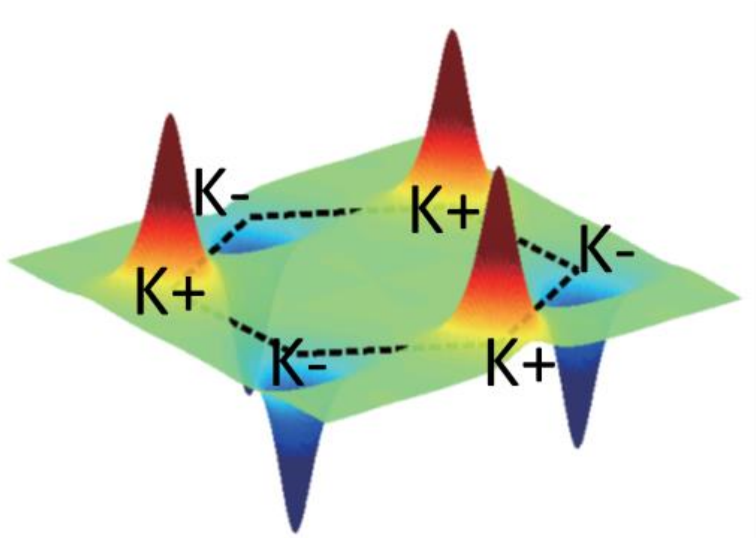
K-
K+
K+
K-
K-
K+

Fig.7.

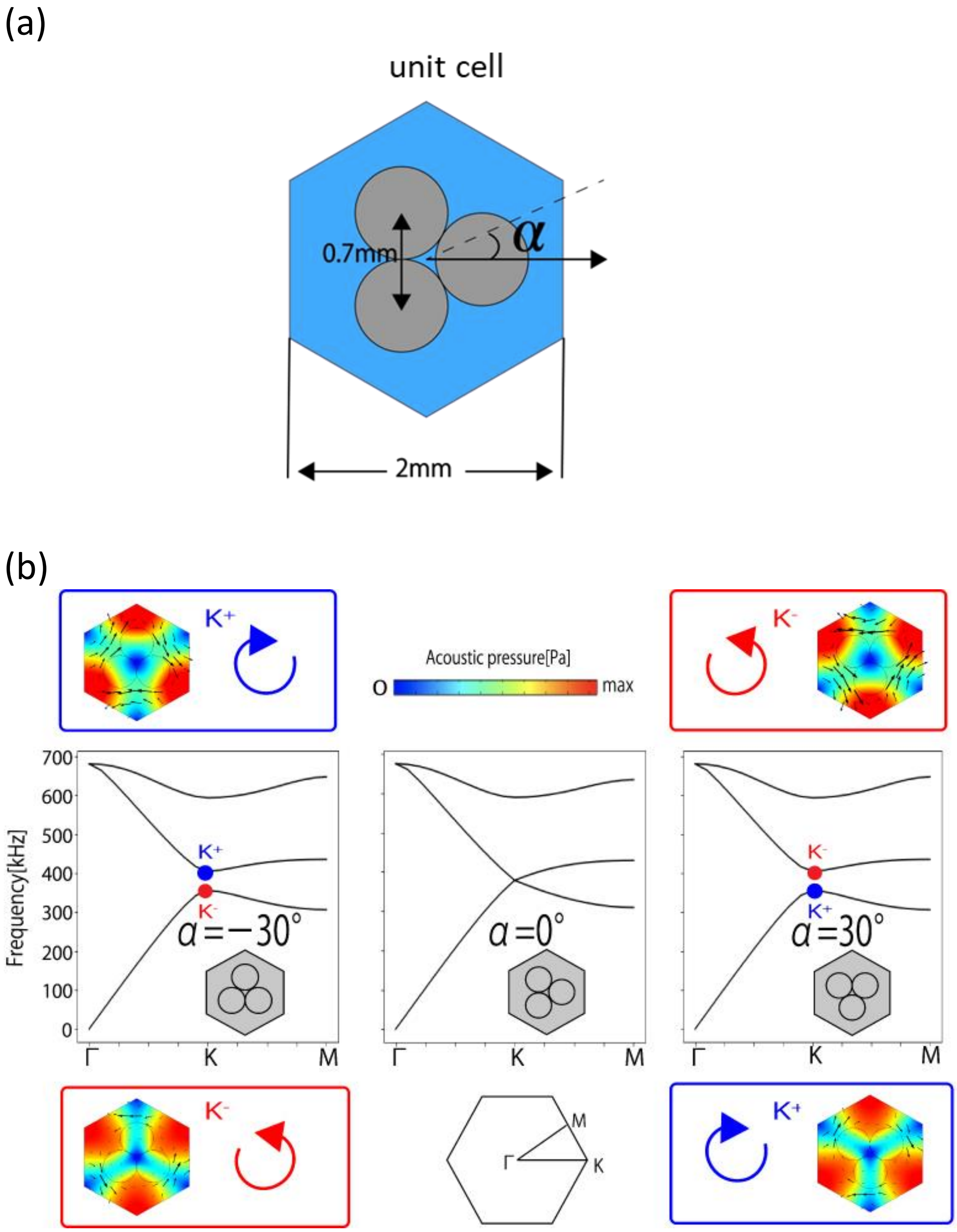
(a)
unit cell
0.7mm
α
2mm
(b)
K+
K-
Acoustic pressure[Pa]
0
max
700
600
500
400
300
200
100
0
Frequency[kHz]
α=−30°
α=0°
α=30°
Γ
K
M

Fig. 8.

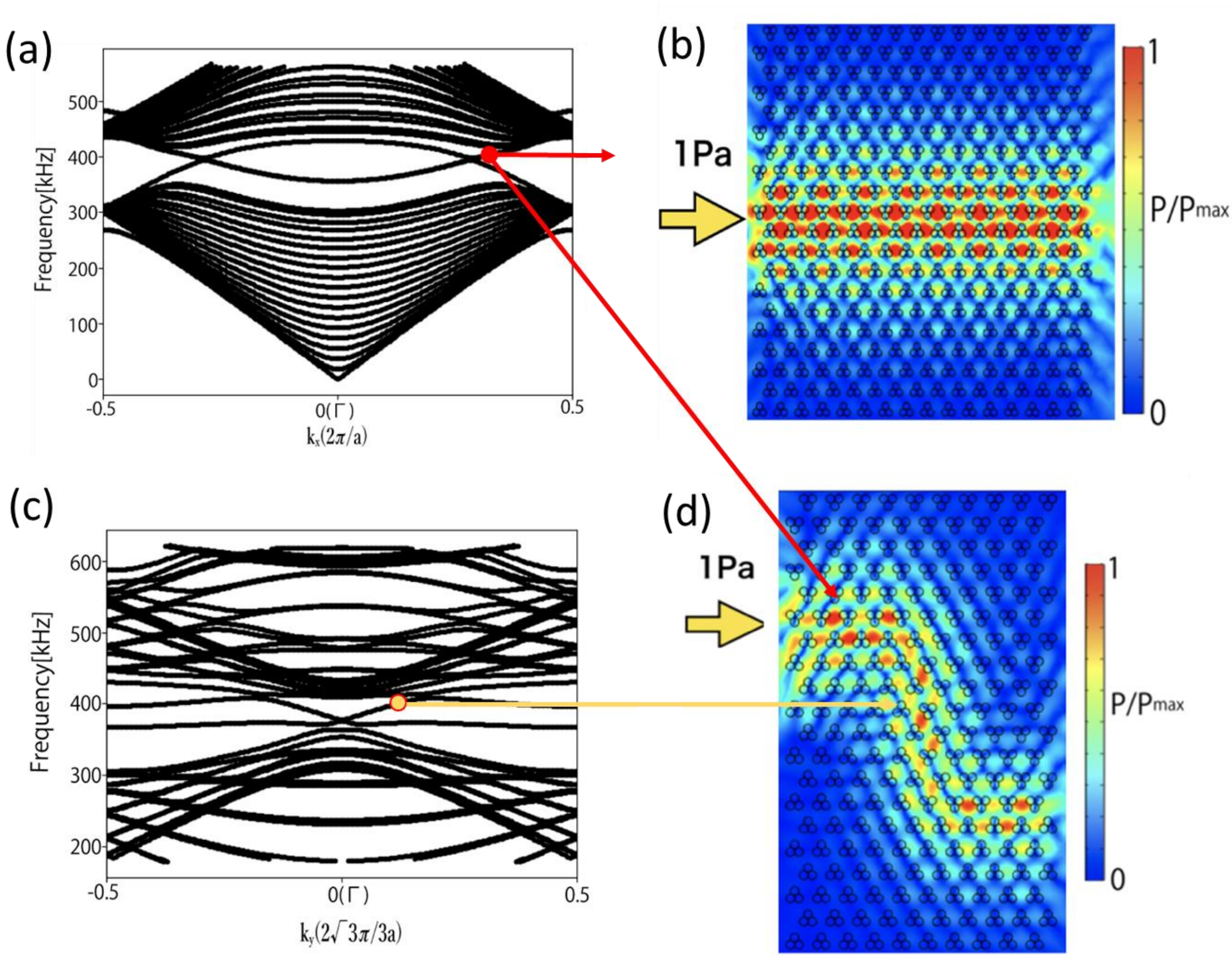
(a)
Frequency[kHz]
$k_x(2\pi/a)$
(b)
1Pa
P/Pmax
1
0
(c)
Frequency[kHz]
$k_y(2\sqrt{3}\pi/3a)$
(d)
1Pa
P/Pmax
1
0

Fig. 9.

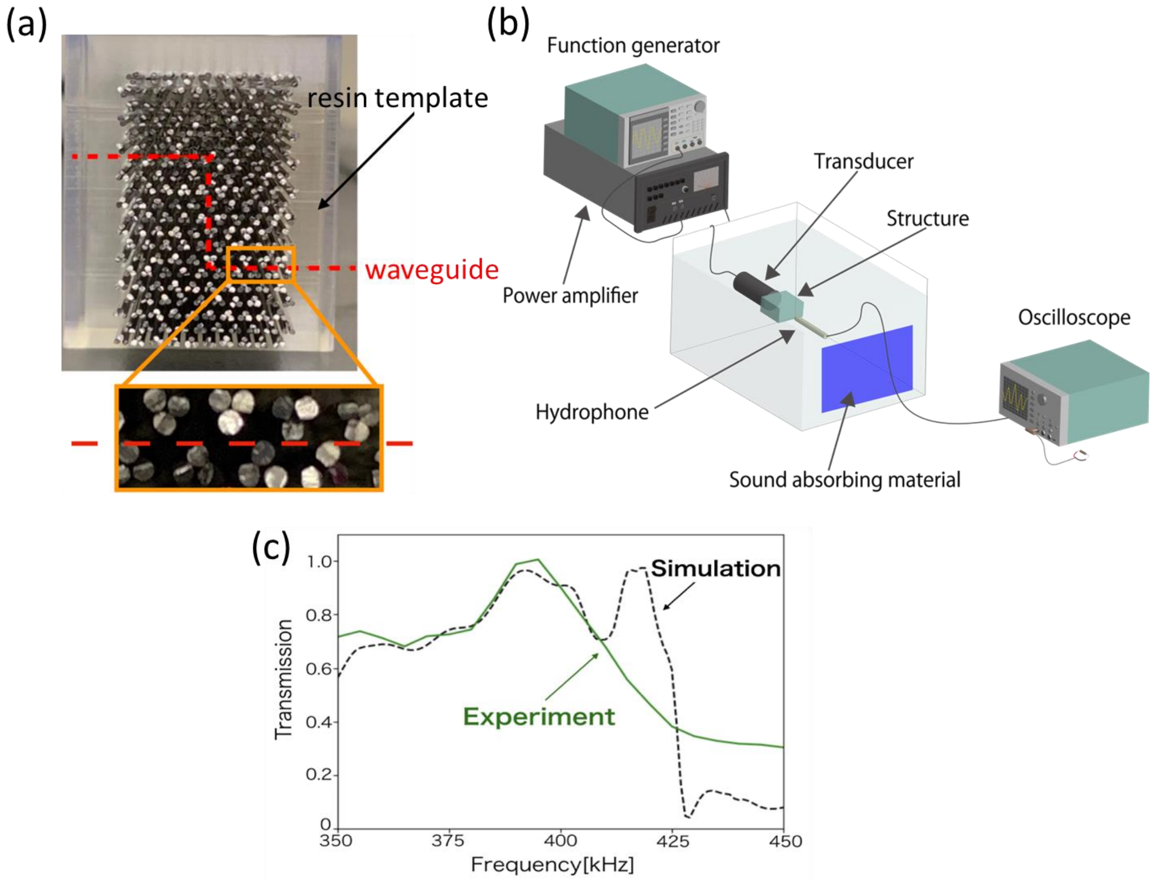
(a)
resin template
waveguide
(b)
Function generator
Transducer
Structure
Power amplifier
Oscilloscope
Hydrophone
Sound absorbing material
(c)
Simulation
Experiment
Transmission
Frequency[kHz]
0
0.2
0.4
0.6
0.8
1.0
350
375
400
425
450

Fig. 10.

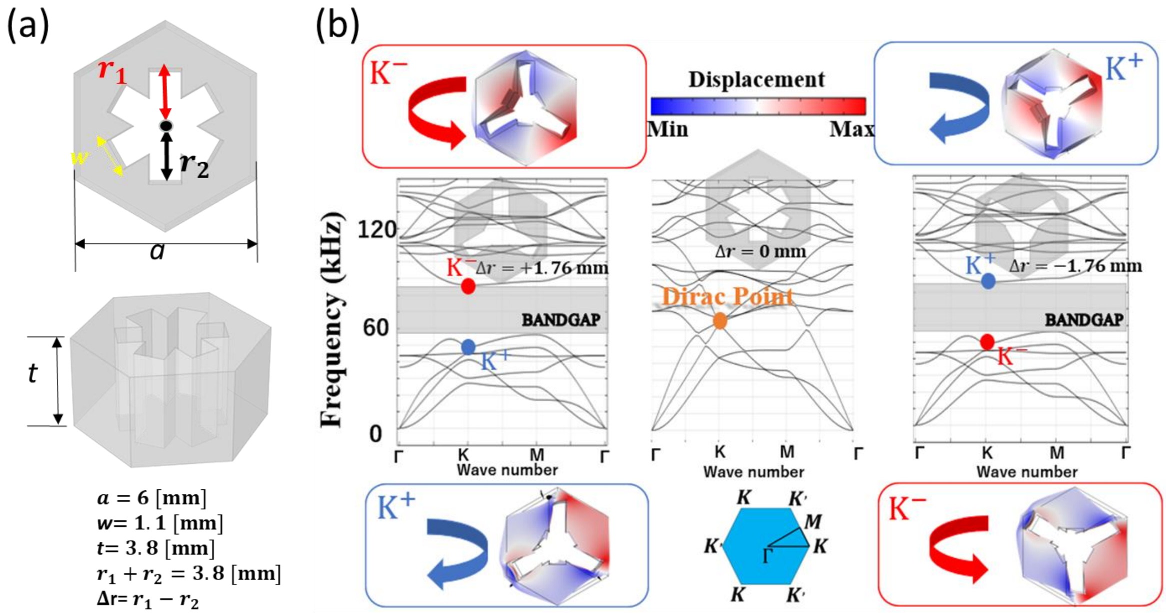
(a)
r_1
w
r_2
a
t
a = 6 [mm]
w= 1. 1 [mm]
t= 3. 8 [mm]
$r_1 + r_2$ = 3. 8 [mm]
Δr= $r_1 - r_2$
(b)
K⁻
Displacement
Min
Max
K⁺
Frequency (kHz)
120
60
0
Δr = +1.76 mm
BANDGAP
Δr = 0 mm
Dirac Point
Δr = −1.76 mm
Γ K M Γ
Wave number
K K' M K Γ

Fig. 11.

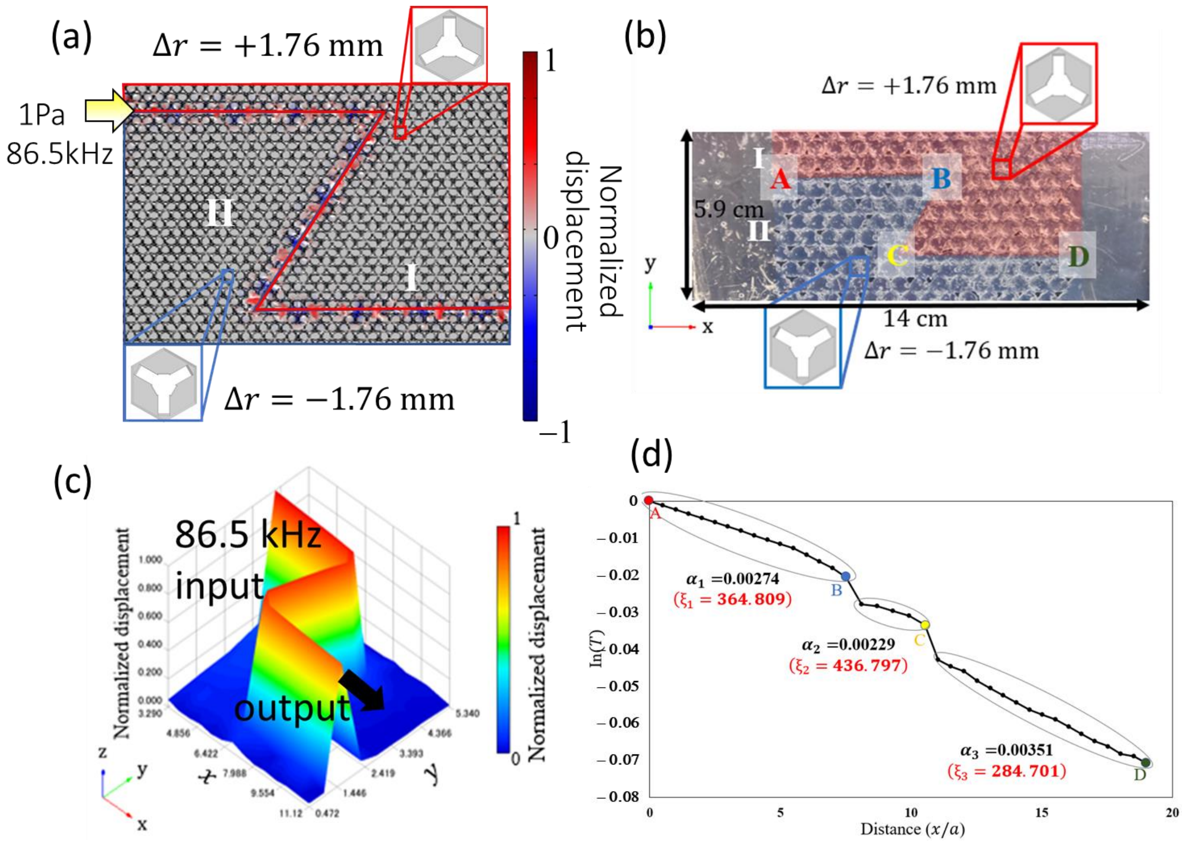
(a)
Δr = +1.76 mm
1Pa
86.5kHz
II
I
Δr = −1.76 mm
Normalized displacement
1
0
−1
(b)
Δr = +1.76 mm
I
A
B
5.9 cm
II
C
D
y
x
14 cm
Δr = −1.76 mm
(c)
86.5 kHz
input
output
Normalized displacement
(d)
α1 =0.00274
(ξ1 = 364.809)
α2 =0.00229
(ξ2 = 436.797)
α3 =0.00351
(ξ3 = 284.701)
ln(T)
Distance (x/a)

Fig. 12.

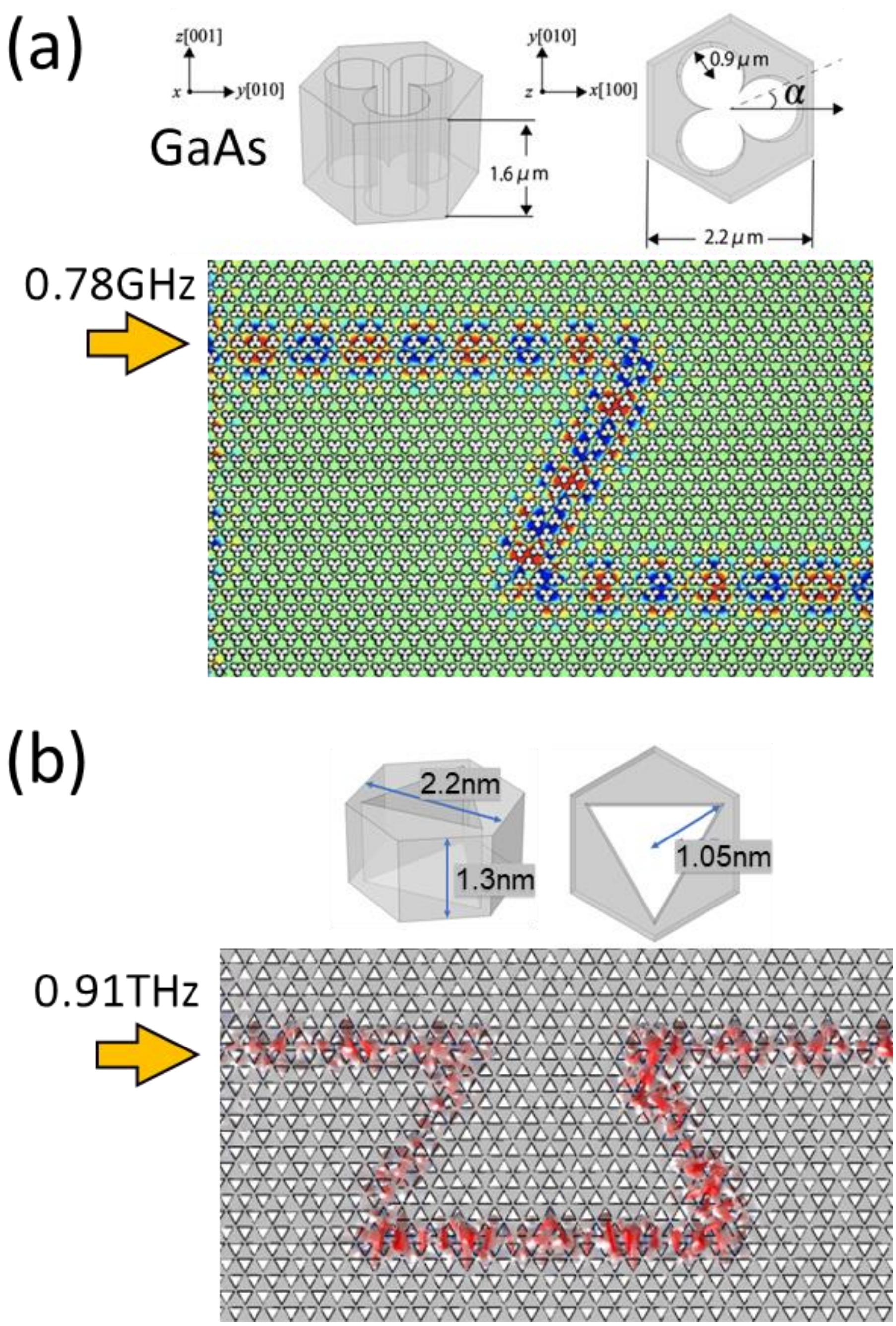
(a)
z[001]
x
y[010]
GaAs
1.6 μm
y[010]
z
x[100]
0.9 μm
α
2.2 μm
0.78GHz
(b)
2.2nm
1.3nm
1.05nm
0.91THz

Fig. 13.